Titre: Title:	Improving the simulation of landfast ice by combining tensile strength and a parameterization for grounded ridges
Auteurs: Authors:	Jean-François Lemieux, Frédéric Dupont, Philippe Blain, François Roy, Gregory C. Smith, & Gregory M. Flato
Date:	2016
Type:	Article de revue / Article
Référence: Citation:	Lemieux, J.-F., Dupont, F., Blain, P., Roy, F., Smith, G. C., & Flato, G. M. (2016). Improving the simulation of landfast ice by combining tensile strength and a parameterization for grounded ridges. Journal of Geophysical Research : Oceans, 121(10), 7354-7368. https://doi.org/10.1002/2016jc012006

Document en libre accès dans PolyPublie
Open Access document in PolyPublie

URL de PolyPublie: PolyPublie URL:	https://publications.polymtl.ca/4997/
Version:	Version officielle de l'éditeur / Published version Révisé par les pairs / Refereed
Conditions d'utilisation: Terms of Use:	CC BY-NC-ND

Document publié chez l'éditeur officiel
Document issued by the official publisher

Titre de la revue: Journal Title:	Journal of Geophysical Research : Oceans (vol. 121, no. 10)
Maison d'édition: Publisher:	AGU Publications
URL officiel: Official URL:	https://doi.org/10.1002/2016jc012006
Mention légale: Legal notice:	© 2016. The Authors. This is an open access article under theterms of the Creative Commons Attribution-NonCommercial-NoDerivsLicense, which permits use anddistribution in any medium, provided the original work is properly cited, the use is non-commercial and no modifications or adaptations are made.

RESEARCH ARTICLE

Improving the simulation of landfast ice by combining tensile strength and a parameterization for grounded ridges

Jean-François Lemieux[1], Frédéric Dupont[2], Philippe Blain[3], François Roy[1], Gregory C. Smith[1], and Gregory M. Flato[4]

[1]Recherche en Prévision Numérique Environnementale, Environnement et Changement Climatique Canada, Dorval, Québec, Canada, [2]Service Météorologique Canadien, Environnement et Changement Climatique Canada, Dorval, Québec, Canada, [3]Département de Génie Physique, École Polytechnique de Montréal, Montréal, Québec, Canada, [4]Canadian Center for Climate Modeling and Analysis, Environment and Climate Change Canada, University of Victoria, Victoria, British Columbia, Canada

Abstract In some coastal regions of the Arctic Ocean, grounded ice ridges contribute to stabilizing and maintaining a landfast ice cover. Recently, a grounding scheme representing this effect on sea ice dynamics was introduced and tested in a viscous-plastic sea ice model. This grounding scheme, based on a basal stress parameterization, improves the simulation of landfast ice in many regions such as in the East Siberian Sea, the Laptev Sea, and along the coast of Alaska. Nevertheless, in some regions like the Kara Sea, the area of landfast ice is systematically underestimated. This indicates that another mechanism such as ice arching is at play for maintaining the ice cover fast. To address this problem, the combination of the basal stress parameterization and tensile strength is investigated using a 0.25° Pan-Arctic CICE-NEMO configuration. Both uniaxial and isotropic tensile strengths notably improve the simulation of landfast ice in the Kara Sea but also in the Laptev Sea. However, the simulated landfast ice season for the Kara Sea is too short compared to observations. This is especially obvious for the onset of the landfast ice season which systematically occurs later in the model and with a slower build up. This suggests that improvements to the sea ice thermodynamics could reduce these discrepancies with the data.

1. Introduction

Landfast ice is sea ice that is immobile or almost immobile near a coast for a certain period of time. It is found in many coastal regions of the Arctic and its peripheral seas. There are a few mechanisms that are thought to play a role in the formation and stabilization of a landfast ice cover. In fall, sea ice formation is fostered in coastal regions because the water is shallow and a warmer subsurface layer is usually absent. Onshore winds can then play a role in the initial stages of landfast ice formation by consolidating and thickening the ice near the shore. In some coastal areas such as in the Beaufort and Laptev Seas, grounded ice ridges might then act as anchor points to stabilize and maintain a landfast ice cover [*Haas et al.*, 2005; *Mahoney et al.*, 2007, 2014].

Landfast ice is important for atmosphere-ice-ocean interactions. As it is immobile, it decreases the transfer of heat, moisture, and momentum between the atmosphere and underlying ocean. Moreover, as the ice is not deforming inside the landfast ice cover, the growth is purely thermodynamically driven [*Johnson et al.*, 2012; *Itkin et al.*, 2015]. Finally, it has been shown that landfast ice impacts the formation of the Arctic cold halocline layer [*Itkin et al.*, 2015].

Despite these important processes, large-scale sea ice models such as CICE [*Hunke and Lipscomb*, 2008] and LIM [*Vancoppenolle et al.*, 2012] do not include some important mechanisms responsible for landfast ice formation and stabilization. To address this issue, we have recently developed a parameterization representing the effect of subgrid-scale grounded ridges on sea ice dynamics. This parameterization, described in *Lemieux et al.* [2015], estimates the largest ridge(s) in a grid cell based on two prognostic model variables: sea ice concentration and mean thickness in a grid cell. When the mean thickness is larger than a critical value that depends on the water depth, the parameterization assumes that a ridge is deep enough to reach the seafloor. A basal stress term is then added to the momentum equation. The maximum basal stress that

can be sustained by the grounded ridge depends on the weight of the ridge in excess of hydrostatic balance. This parameterization is simple and easy to implement in both two-thickness category and multithickness category models. Pan-Arctic experiments have shown that adding the parameterization leads to more realistic simulated landfast ice covers in regions such as the East Siberian Sea, the Laptev Sea, and along the coast of Alaska. However, in some regions such as the Kara Sea, *Lemieux et al.* [2015] have shown that the model systematically underestimates the area of landfast ice (even with the basal stress parameterization). As the Kara Sea is overall deeper than coastal regions of the East Siberian and Laptev Seas, the grounding scheme is less active as most parameterized ridges are not able to reach the seafloor. This indicates that another mechanism is involved to maintain the ice fast in this region.

In a recent study, *Ólason* [2016] suggested that ice arching is the main mechanism responsible for maintaining a landfast ice cover in the Kara Sea. He argues that the arches take footing on chains of islands located offshore. This is consistent with the observations of *Divine et al.* [2005] indicating that a series of archipelagos contribute to the stabilization of the Kara Sea landfast ice cover. Ice arches at the offshore landfast ice edge have also been observed elsewhere such as in the Bay of Bothnia [*Goldstein et al.*, 2004].

It is well known that to develop stable arches, a material (in our case sea ice) needs to be able to sustain tensile stresses [e.g., *Dumont et al.*, 2009]. The most common representation of rheology in current sea ice models is based on a viscous-plastic formulation with an elliptical yield curve [*Hibler*, 1979]. *Ip* [1993] demonstrated that the viscous-plastic rheology can simulate ice arches, provided that it has tensile strength. With the standard ellipse parameters, simulated sea ice cannot support isotropic tensile stresses but has, however, some resistance to uniaxial tension. *Dumont et al.* [2009] were able to simulate the North Water polynya ice bridge by increasing the amount of uniaxial tensile strength of the elliptical yield curve.

The main objective of this paper is to investigate how simulations of landfast ice can be improved by combining a yield curve with tensile strength and a grounding scheme for pressure ridges. The impact of both isotropic and uniaxial tensile strengths is investigated by conducting Pan-Arctic simulations. Following *König Beatty and Holland* [2010], we modify the viscous-plastic rheology with an elliptical yield curve to include isotropic tensile strength. Moreover, as *Dumont et al.* [2009], we decrease the ellipse aspect ratio to increase the uniaxial tensile strength. We assess the quality of the simulated landfast ice over many regions with a special focus on the Kara Sea where ice arching is thought to be important [*Ólason*, 2016].

The contributions of this paper are: a description of the implementation of isotropic tensile strength in the CICE model (including the replacement pressure), a description of the implementation of the *Lemieux et al.* [2015] grounding scheme on a B-grid (CICE), and a thorough investigation of the simulated landfast ice cover in Pan-Arctic experiments when combining tensile strength and the grounding scheme.

This paper is structured as follows. Section 2 describes the sea ice momentum equation with the basal stress parameterization and the modified rheology. A description of the numerical implementation is given in section 3. Information about the ice-ocean model and the forcing used for the experiments is provided in section 4. The results of the numerical experiments are presented in section 5. Broader implications are considered in section 6. The conclusion and a description of future work are provided in section 7.

2. Modified Sea Ice Momentum Equation

For the numerical experiments, we use the CICEv4.0 sea ice model [*Hunke and Lipscomb*, 2008] coupled to the NEMO ocean model [*Megann et al.*, 2014]. Here is a description of the modified sea ice momentum equation that includes isotropic tensile strength and the grounding scheme.

The two-dimensional sea ice momentum equation is given by

$$m\frac{D\mathbf{u}}{Dt} = -\mathbf{k} \times mf\mathbf{u} + \boldsymbol{\tau}_a + \boldsymbol{\tau}_w + \boldsymbol{\tau}_b + \nabla \cdot \boldsymbol{\sigma} - mg\nabla H_o, \tag{1}$$

where m is the combined mass of ice and snow per unit area, $\frac{D}{Dt}$ is the total derivative, t is the time, f is the Coriolis parameter, $\mathbf{u} = u\mathbf{i} + v\mathbf{j}$ is the horizontal sea ice velocity vector, $\mathbf{i}$, $\mathbf{j}$, and $\mathbf{k}$ are unit vectors aligned with the x, y, and z axis of the coordinate system, $\boldsymbol{\tau}_a = \tau_{ax}\mathbf{i} + \tau_{ay}\mathbf{j}$ is the wind stress, $\boldsymbol{\tau}_w = \tau_{wx}\mathbf{i} + \tau_{wy}\mathbf{j}$ is the water stress, $\boldsymbol{\tau}_b = \tau_{bx}\mathbf{i} + \tau_{by}\mathbf{j}$ is a basal stress term due to grounded ridges, $\boldsymbol{\sigma}$ is the internal ice stress tensor with components $\sigma_{11} = \sigma_{xx}$, $\sigma_{22} = \sigma_{yy}$, and $\sigma_{12} = \sigma_{xy}$, g is the gravitational acceleration, and H_o the sea surface height.

In CICE, the advection of momentum is neglected. In our implementation, the stresses τ_a and τ_w are formulated as in *Roy et al.* [2015]. Following *Lemieux et al.* [2015], the basal stress τ_b is given by

$$\tau_{\mathbf{b}} = \begin{cases} 0 & \text{if } h \leq h_c, \\ k_2 \left(\dfrac{-\mathbf{u}}{|\mathbf{u}| + u_0} \right)(h - h_c)\exp^{-\alpha_b(1-A)} & \text{if } h > h_c, \end{cases} \tag{2}$$

where h is the mean thickness in a grid cell (or volume per unit area), h_c the critical mean thickness, k_2 a free parameter that determines the maximum basal stress, A the ice concentration, $|\mathbf{u}| = \sqrt{u^2 + v^2}$, u_0 a small velocity parameter, and α_b the basal stress ice concentration parameter. The critical thickness h_c is equal to Ah_w/k_1 where k_1 is the critical thickness parameter and h_w is the bathymetry defined as positive downward. The τ_b formulation in equation (2) indicates that the basal stress is zero when $h \leq h_c$, or in other words that the parameterized ridge is not deep enough to reach the seafloor.

CICE is based on a viscous-plastic (VP) rheology with an elliptical yield curve [*Hibler*, 1979]. The momentum equation is solved with the elastic-VP (EVP) approach [*Hunke*, 2001]. With this method, the stresses are subcycled between two time levels following

$$\frac{\partial \sigma_1}{\partial t} + \frac{\sigma_1}{2T_d} + \frac{p}{2T_d} = \frac{\zeta}{T_d} D_D, \tag{3}$$

$$\frac{\partial \sigma_2}{\partial t} + \frac{e^2 \sigma_2}{2T_d} = \frac{\zeta}{T_d} D_T, \tag{4}$$

$$\frac{\partial \sigma_{12}}{\partial t} + \frac{e^2 \sigma_{12}}{2T_d} = \frac{\zeta}{2T_d} D_S, \tag{5}$$

where $\sigma_1 = \sigma_{11} + \sigma_{22}$, $\sigma_2 = \sigma_{11} - \sigma_{22}$, $D_D = \frac{\partial u}{\partial x} + \frac{\partial v}{\partial y}$, $D_T = \frac{\partial u}{\partial x} - \frac{\partial v}{\partial y}$, $D_S = \frac{\partial u}{\partial y} + \frac{\partial v}{\partial x}$, p is a pressure-like term, T_d is the damping time scale for elastic waves, ζ is the bulk viscous coefficient, and e is the ratio of the major and minor axes of the elliptical yield curve, sometimes referred to as the ellipse aspect ratio. Note that σ_1 and σ_2 should not be confused with the principal stresses which are denoted by σ_{p1} and σ_{p2} in this article. The principal stresses are the components of the stress tensor when the coordinate system is rotated in such a way that the shear stress vanishes. The principal stresses, which correspond to the maximum and minimum normal stresses, are given by

$$\sigma_{p1}, \sigma_{p2} = \frac{\sigma_{11} + \sigma_{22}}{2} \pm \sqrt{\left(\frac{\sigma_{11} - \sigma_{22}}{2} \right)^2 + \sigma_{12}^2}. \tag{6}$$

Based on *König Beatty and Holland* [2010], isotropic tensile strength is introduced by letting $\zeta = P_p(1 + k_t)/2\Delta^*$ and $p = (1 - k_t)P$ in equations (3–5) where P_p is the compressive ice strength parameterized following *Lipscomb et al.* [2007], $\Delta^* = \max(\Delta, \Delta_{min})$ with $\Delta = \left[D_D^2 + e^{-2}(D_T^2 + D_S^2) \right]^{\frac{1}{2}}$ and where Δ_{min} is a small deformation to prevent a singularity on ζ when Δ tends toward zero, k_t is a parameter that characterizes the amount of tensile strength (herein T) as a function of the ice strength in compression ($T = k_t P_p$), and $P = P_p\Delta/\Delta^*$ is a replacement pressure to ensure the internal stresses are zero when the strain rates are zero.

To visualize the impact of e and k_t on the elliptical yield curve, three different yield curves (normalized by the ice strength) are plotted in principal stress space in Figure 1. Tensile stresses are by convention positive. The standard yield curve ($e = 2$ and $k_t = 0$, black curve) only exhibits small uniaxial tensile strength (only one principal stress can be positive). Larger uniaxial tensile stresses can be sustained by the ice by decreasing the value of e (magenta curve). Only the ellipse with $k_t > 0$ allows both σ_{p1} and σ_{p2} to be positive, i.e., the ice has isotropic tensile strength.

3. Numerical Implementation

We wish to solve the momentum equation at time levels $\Delta t, 2\Delta t, 3\Delta t, \ldots$ where $n = 1, 2, 3, \ldots$ identifies the time level and Δt is referred to as the advective time step. With the EVP method, the momentum equation is integrated explicitly from $n - 1$ to n. N_{sub} subcycles are performed such that $N_{sub}\Delta t_e = \Delta t$ where Δt_e is the EVP subcycling time step. The elastic damping time scale and Δ_{min} are set to the default values in CICE (i.e., $T_d = 0.36 \Delta t$
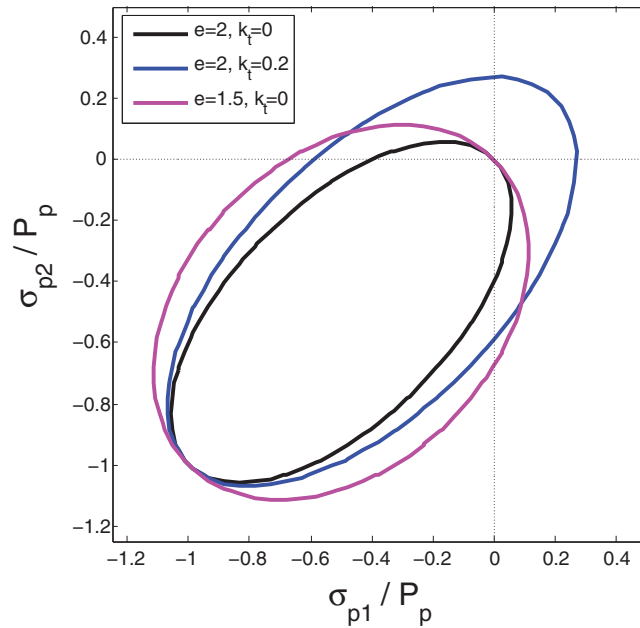
Figure 1. Elliptical yield curves with parameters $e = 2$, $k_t = 0$ (in black), $e = 2$, $k_t = 0.2$ (in blue), and $e = 1.5$, $k_t = 0$ (in magenta).

and $\Delta_{min} = 10^{-11}$ s^{-1}). At subcycle s, the internal stresses σ_1, σ_2, and σ_{12} are first advanced in time by solving explicitly the following equations

$$\frac{\sigma_1^s - \sigma_1^{s-1}}{\Delta t_e} + \frac{\sigma_1^s}{2T_d} + \frac{P(1-k_t)}{2T_d} = \frac{P_p(1+k_t)}{2\Delta^{*s-1}T_d}D_D^{s-1},$$
(7)

$$\frac{\sigma_2^s - \sigma_2^{s-1}}{\Delta t_e} + \frac{e^2\sigma_2^s}{2T_d} = \frac{P_p(1+k_t)}{2\Delta^{*s-1}T_d}D_T^{s-1}, \quad (8)$$

$$\frac{\sigma_{12}^s - \sigma_{12}^{s-1}}{\Delta t_e} + \frac{e^2\sigma_{12}^s}{2T_d} = \frac{P_p(1+k_t)}{4\Delta^{*s-1}T_d}D_S^{s-1}.$$
(9)

The u and v components of velocity are then advanced in time by solving explicitly the equations

$$m\frac{(u^s - u^{s-1})}{\Delta t_e} + C_b u^s - mfv^s =$$

$$\tau_{ax} + \tau_{wx} - mg\frac{\partial H_o}{\partial x} + \frac{\partial \sigma_{11}^s}{\partial x} + \frac{\partial \sigma_{12}^s}{\partial y},$$
(10)

$$m\frac{(v^s - v^{s-1})}{\Delta t_e} + C_b v^s + mfu^s = \tau_{ay} + \tau_{wy} - mg\frac{\partial H_o}{\partial y} + \frac{\partial \sigma_{22}^s}{\partial y} + \frac{\partial \sigma_{21}^s}{\partial x},$$
(11)

where C_b is the basal stress coefficient. More details on the treatment of τ_a, τ_w, and the ocean tilt term can be found in *Hunke and Lipscomb* [2008].

When the ridge is too small to reach the seafloor, the basal stress should be zero. In this case $C_b = 0$. However, when the mean thickness is larger than the critical one, the basal stress coefficient is given by

$$C_b = \left(\frac{k_2}{\sqrt{(u^{s-1})^2 + (v^{s-1})^2 + u_0}}\right)(h_u - h_{cu})\exp^{-\alpha_b(1-A_u)},$$
(12)

with the subscript u indicating that h_u, A_u, and $h_{cu} = A_u h_{wu}/k_1$ are defined at the u (and v) location. As CICE is based on an Arakawa B-grid, the mean thickness (h), concentration (A), and bathymetry (h_w) are defined at the tracer point (center of the cell) while u and v are defined at the nodes (corners). Instead of a simple bilinear interpolation to get h_u, A_u and h_{wu}, these quantities are given by $h_u = \max[h_{ij}, h_{ij+1}, h_{i+1j+1}, h_{i+1j}]$, $A_u = \max[A_{ij}, A_{ij+1}, A_{i+1j+1}, A_{i+1j}]$ and $h_{wu} = \min[h_{wij}, h_{wij+1}, h_{wi+1j+1}, h_{wi+1j}]$. *Lemieux et al.* [2015] argued that this way of calculating h_u, A_u, and h_{wu} leads to a more stable and more realistic landfast ice cover than a bilinear interpolation.

This approach is easy to implement numerically as the basal stress term is similar to the water stress term (see *Hunke and Lipscomb* [2008] for details). Note that to avoid unnecessary calculations where there is little ice, the C_b are computed only where $A_u > 0.01$.

4. Experimental Setup

Pan-Arctic simulations are conducted with an ice-ocean model. The ocean component is NEMO version 3.1 with minor modifications [*Dupont et al.*, 2015]. As mentioned above, the sea ice model is CICE version 4.0 with some modifications that include the UK Met Office NEMO-CICE interface [*Megann et al.*, 2014]. The domain, shown in Figure 2, covers the Arctic and the North Atlantic. The regional grid is a subset of the 0.25° global ORCA mesh. This correspond to a spatial resolution of ∼12.5 km in the central Arctic. Ice-ocean simulations are forced by 33 km resolution atmospheric reforecasts from Environment Canada [*Smith et al.*, 2014].
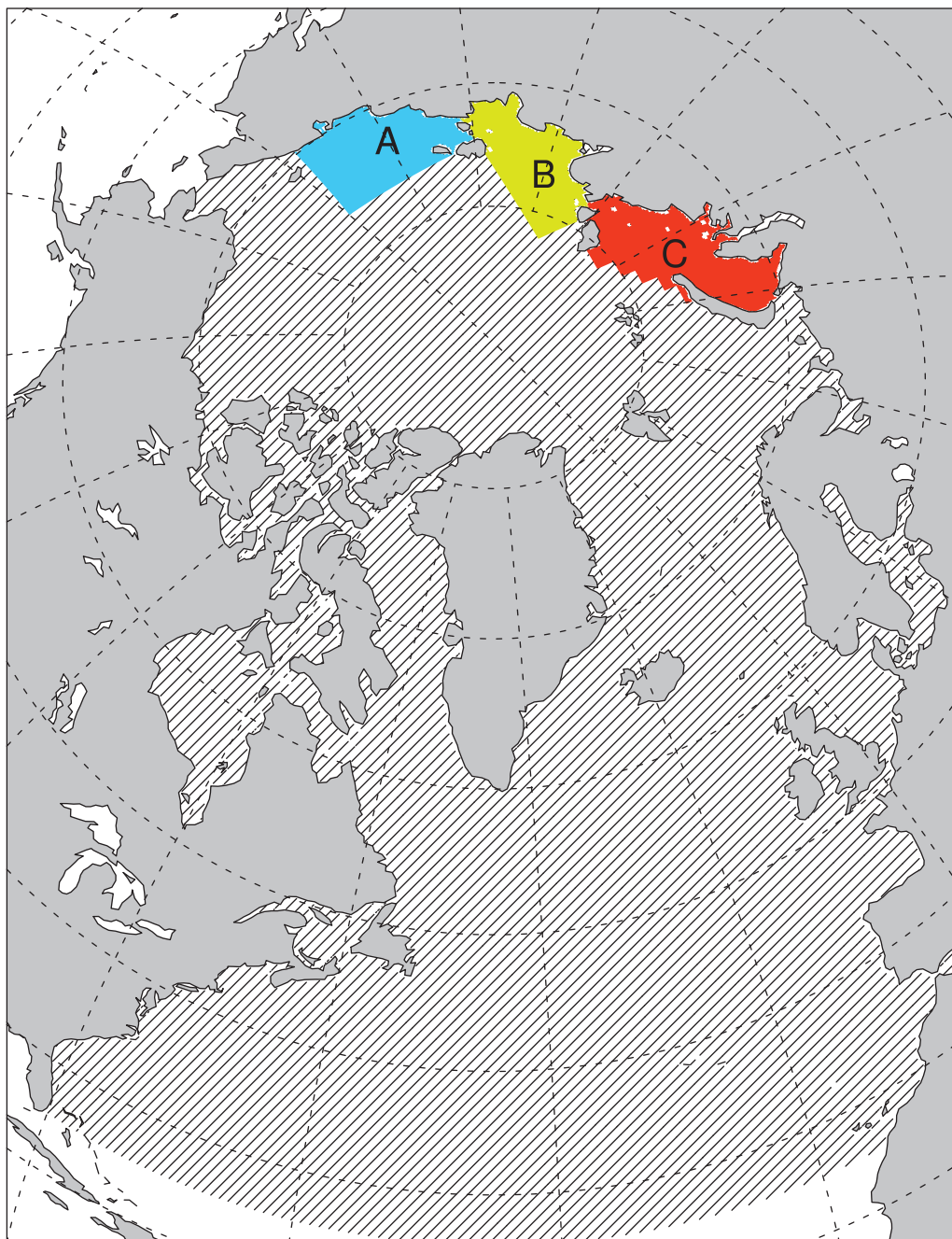
Figure 2. The domain covered (hatched area) by the 0.25° Pan-Arctic grid used for the simulations. Regions used to calculate landfast ice area are shown in color. The East Siberian Sea region is in light blue (A), the Laptev Sea region is in yellow (B), and the Kara Sea region is in red (C).

As in *Lemieux et al.* [2015], we use the National Ice Center (NIC) 25 km gridded landfast ice data [*National Ice Center*, 2006]. This Pan-Arctic data set identifies grid cells that are covered by landfast ice. Unfortunately, the NIC data set ends in 2007. As the Environment Canada forcing data set is only available for the period 2001–2011, we decided to create a spin-up from January 2001 to September 2004 and to analyze a series of simulations between September 2004 and September 2007.

For the period covered by our simulations, the NIC ice charts were produced biweekly. As mentioned by *Yu et al.* [2014], the accuracy of the NIC ice data is affected by the use of a mix of data sources and the transformation of the charts into gridded products. As the charts are manually produced, the uncertainties also depend on the skill of each ice analyst. By comparing the seaward landfast ice edge in the

Table 1. Tensile Strength and Basal Stress Parameters for the Simulations

Symbol	Definition	Value
e	Ellipse aspect ratio	1.2, 1.4, 1.6, 1.8, 2.0
k_t	Isotropic tensile strength parameter	0.0, 0.1, 0.2, 0.3, 0.4
k_1	Critical thickness parameter	8
k_2	Maximum basal stress parameter	15 N m^{-3}
α_b	Basal stress ice concentration parameter	20
u_0	Basal stress velocity parameter	5×10^{-5} m s^{-1}

Beaufort Sea from the NIC ice charts to the one obtained from RADARSAT imagery, *Yu et al.* [2014] tried to estimate this uncertainty. They found differences between -15 and 1.5 km with an overall mean of -6.5 km and a standard deviation of 13.6 km. They nevertheless concluded that it is difficult if not impossible to correctly quantify the uncertainty. To minimize the uncertainty in their analysis, they focused on large-scale patterns and time averages of landfast ice extents. We also follow this approach.

The model was initialized with sea ice concentration and thickness fields from the Glorys2v1 ocean reanalysis [*Ferry et al.*, 2012]. Initial and boundary conditions for the ocean are taken from the Mercator Océan ORCA12-T321 simulation (as done by *Dupont et al.* [2015]). Ocean inflow at Bering Strait is imposed based on this simulation while for sea ice, Bering Strait is treated as a closed boundary. The spin-up simulation was conducted without the basal stress parameterization and with the standard elliptical yield curve.

Numerical experiments focus on the aspect ratio e and on the isotropic tensile strength parameter k_t, with the basal stress parameters k_1 and k_2 held constant. *Lemieux et al.* [2015] performed a sensitivity study of the simulated landfast ice area in different regions as a function of k_1 and k_2. They showed that $k_1=8$ and $k_2=15$ N m^{-3} lead to quite realistic simulations of landfast ice in the East Siberian, Laptev, and Beaufort Seas. Despite a different model setup, the same basal stress parameter values are used here. In some figures of this article, the label "grounding" is used for simulations conducted with the grounding scheme with $k_1=8$ and $k_2=15$ N m^{-3}. Table 1 lists the values of the fixed basal stress parameters and the tensile strength parameters tested in the simulations. All other CICE physical parameters are set to the default values [*Hunke and Lipscomb*, 2008].

The advective time step Δt is 10 min for all the simulations. Following the work of *König Beatty and Holland* [2010] and our own experience with the EVP solver, we have increased the number of subcycling iterations (N_{sub}) in order to improve the numerical convergence of the solution. The impact is illustrated in Figure 3 which shows the simulated area of landfast ice in the Kara region as a function of time (only the first year is shown) for different values of N_{sub}. Increasing N_{sub} from 120 to 920 improves the convergence of the solution and overall enhances the simulated area of landfast ice. It is possible that a larger value of N_{sub} would lead to a slightly more extended landfast ice cover. However, to limit the computational cost, the simulations were conducted with $N_{sub} = 920$.
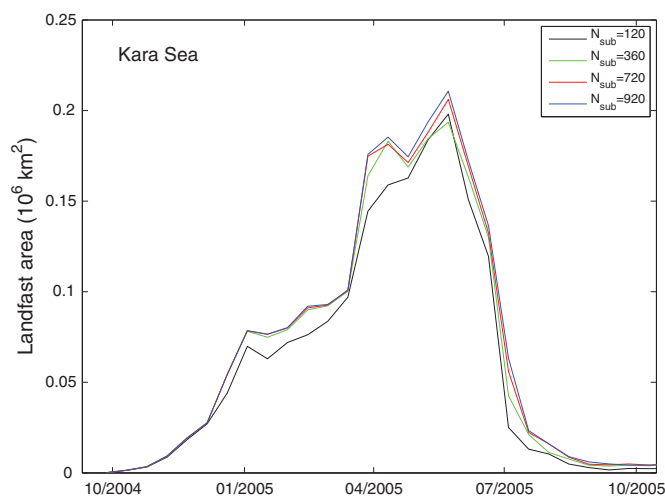

Figure 3. Simulated area of landfast ice in the Kara Sea as a function of time for 120 (black), 360 (green), 720 (red), and 920 (blue) EVP subcycles. For all these simulations, $e = 2.0$, $k_t = 0.2$, and the grounding scheme was used.

5. Results

Outputs from our simulations are daily mean values defined at tracer points. From the mean daily ice velocity $\mathbf{u}_d = u_d\mathbf{i} + v_d\mathbf{j}$, we calculate the ice speed $(u_d^2 + v_d^2)^{\frac{1}{2}}$ at each grid cell. Similar to *Lemieux et al.* [2015], ice at a certain grid cell is considered landfast if its 2 week mean speed is smaller than 5×10^{-4} m s^{-1}. A 2 week window is used to define landfast ice as a shorter period could lead to false assessments for low wind events. The area of landfast ice for a certain region (regions are shown in Figure 2) is calculated every 2 weeks by summing the area of landfast cells. Simulated landfast ice is compared
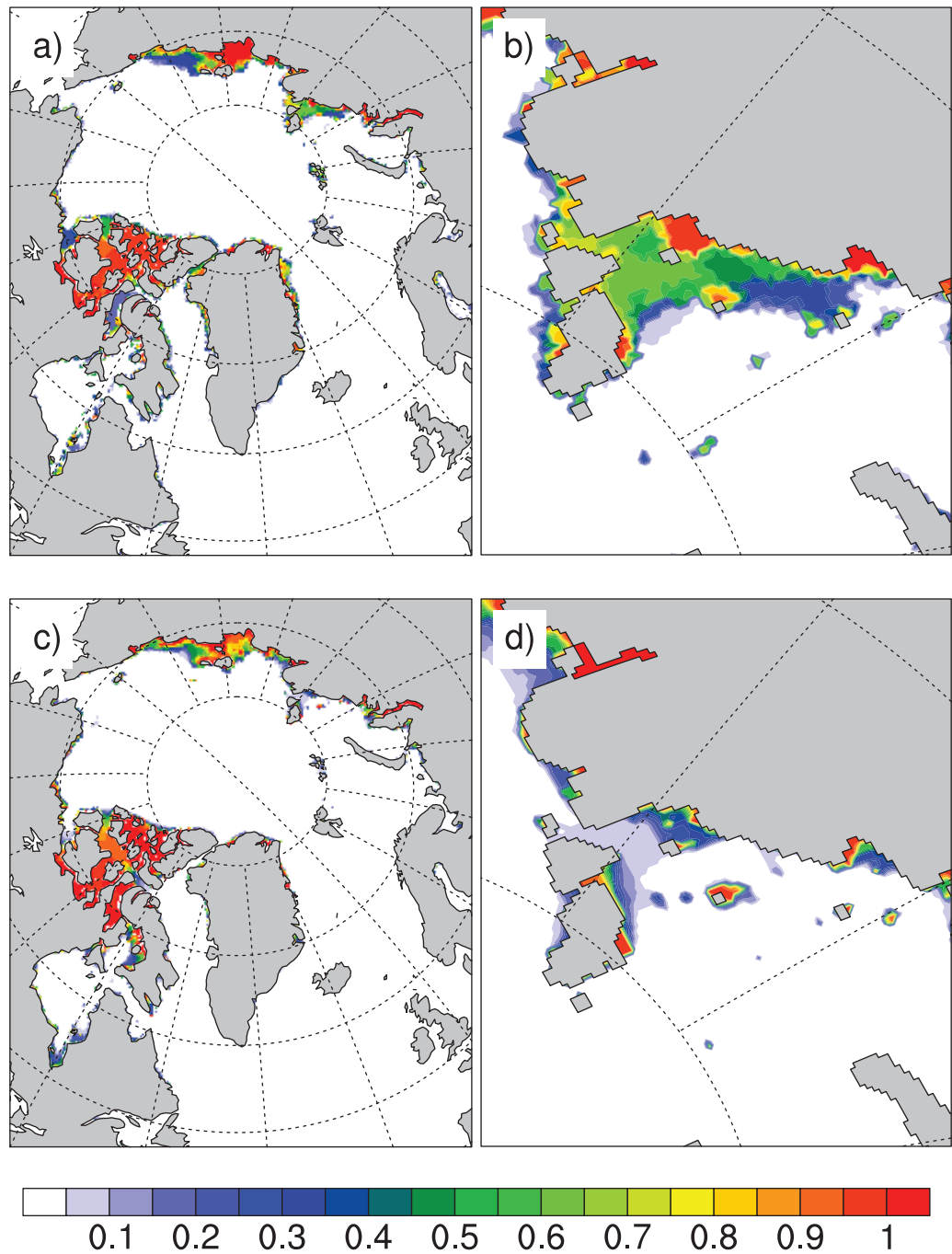
Figure 4. Frequency of occurrence of landfast ice for January–May for the years 2005, 2006, and 2007. NIC observations over the whole domain (a), zoom of NIC observations in the eastern part of the Kara Sea (b), simulation with grounding over the whole domain (c), and zoom of the simulation with grounding in the eastern part of the Kara Sea (d).

with the NIC data. To do so, the observations are interpolated to the model grid using a nearest neighbor approach.

Similar to *Yu et al.* [2014], we calculate the frequency of occurrence of landfast ice for the data and the simulations for January–May for the years 2005, 2006, and 2007. Figure 4 compares the frequency of occurrence for the model with the grounding scheme and the standard yield curve and the one from the observations. As for the model of *Lemieux et al.* [2015], CICE with the basal stress parameterization leads to quite realistic simulations of landfast ice in many regions such as the East Siberian, the Beaufort, and to some extent in
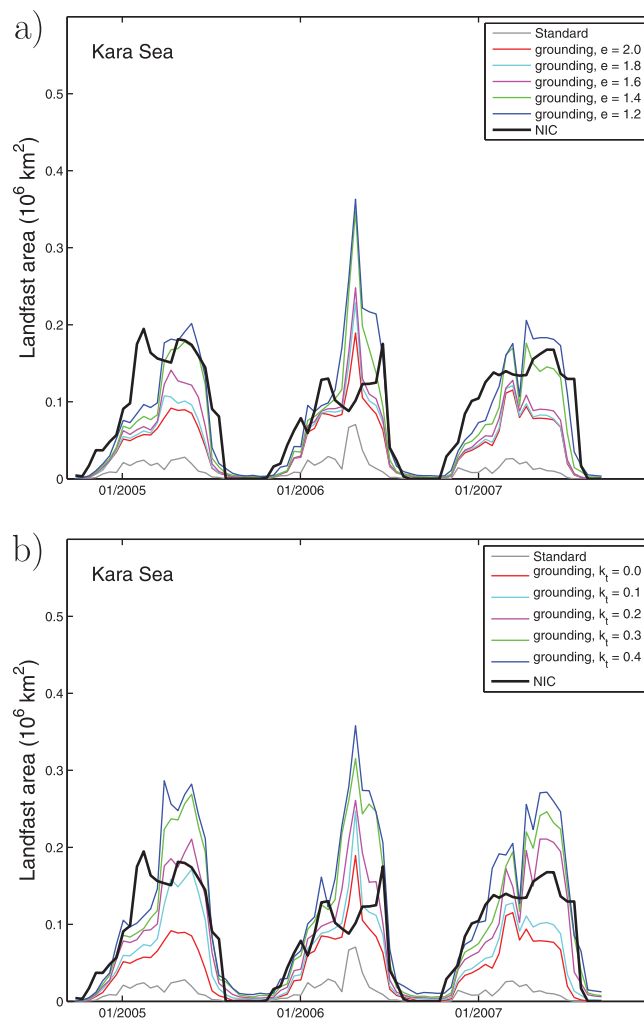
Figure 5. Impact of uniaxial tensile strength on the simulated area of landfast ice in the Kara Sea as a function of time. The gray curve is for the standard model ($e = 2$, $k_t = 0$, no grounding scheme). The red, cyan, magenta, green, and blue curves are, respectively, for $e=2.0, 1.8, 1.6, 1.4$, and 1.2 (with grounding and $k_t = 0$). The bold black curve displays the area calculated from the NIC data (a). Impact of isotropic tensile strength on the simulated area of landfast ice in the Kara Sea as a function of time. The red, cyan, magenta, green, and blue curves are, respectively, for $k_t = 0.0, 0.1, 0.2, 0.3$, and 0.4 (with grounding and $e = 2$) (b).

the Laptev Sea. In the Canadian Arctic Archipelago, where the ice is land-locked, the model simulates the land-fast ice quite well. However, in the Kara Sea, the frequency of occurrence for the simulated landfast ice is clearly lower than what is observed (Figure 4d).

We now investigate how the simulated landfast ice cover can be improved in the Kara Sea (and Laptev Sea as will be shown) when increasing uniaxial tensile strength or adding isotropic tensile strength. We also assess how these modifications to the sea ice rheology affect the simulated landfast ice cover in other regions. Figure 5a displays the sensitivity of the simulated landfast ice area in the Kara Sea to different values of the ellipse aspect ratio e. The standard simulation was obtained with $e = 2$, $k_t = 0$ and without the basal stress parameterization. As in *Lemieux et al.* [2015], the simulated landfast ice area is systematically underestimated with the standard model (gray curve) and when using only the grounding scheme (red curve). As expected, decreasing e (i.e., increasing uniaxial tensile strength) enhances the landfast ice area.

To assess what parameter values provide the best fit to the data, we calculated the mean simulated ($\bar{a}_s$) and observed ($\bar{a}_o$) landfast ice area between January and May for the three landfast ice seasons. The metric used to evaluate the quality of a simulation is the mean (over the three seasons) of the absolute error $\bar{a}_s$-$\bar{a}_o$, that is $\frac{1}{3}\sum_{n=1}^{3}|\bar{a}_s^n - \bar{a}_o^n|$ where the superscript $n = 1$, 2, and 3 refer to the three landfast ice seasons. Using this approach, we conclude that an ellipse ratio between $e = 1.4$ and $e = 1.2$ provides the best fit. Similarly, as seen in Figure 5b, larger values of k_t (i.e., increasing isotropic tensile strength) lead to a larger landfast ice area, with $k_t = 0.2$ providing the best fit to the data. Values of $k_t > 0.2$ result in a systematic overestimation of the landfast ice extent (late winter and spring).

Nevertheless, with these optimal parameters, the model clearly overestimates the extent of landfast ice during a short period in 2006. Indeed, on 24 April 2006, the simulated landfast ice cover extends all the way to Novaya Zemlya while this is not seen in the observations. This is what explains the large peak in Figure 5a (with $e = 1.4$ for example). We do think, however, that sea ice at this location should not have been identified as landfast. Over the 3 year period, it is the only time landfast ice is simulated in this region. Furthermore, based on the NIC data, landfast ice has never been observed there during the same period. This points to a limitation of our method (and criterion) to determine whether the simulated ice is landfast or not. In other words, sea ice in this region should have been identified as slow drifting instead of landfast ice. This indicates that it would be beneficial to develop more sophisticated verification methods for simulated landfast ice.
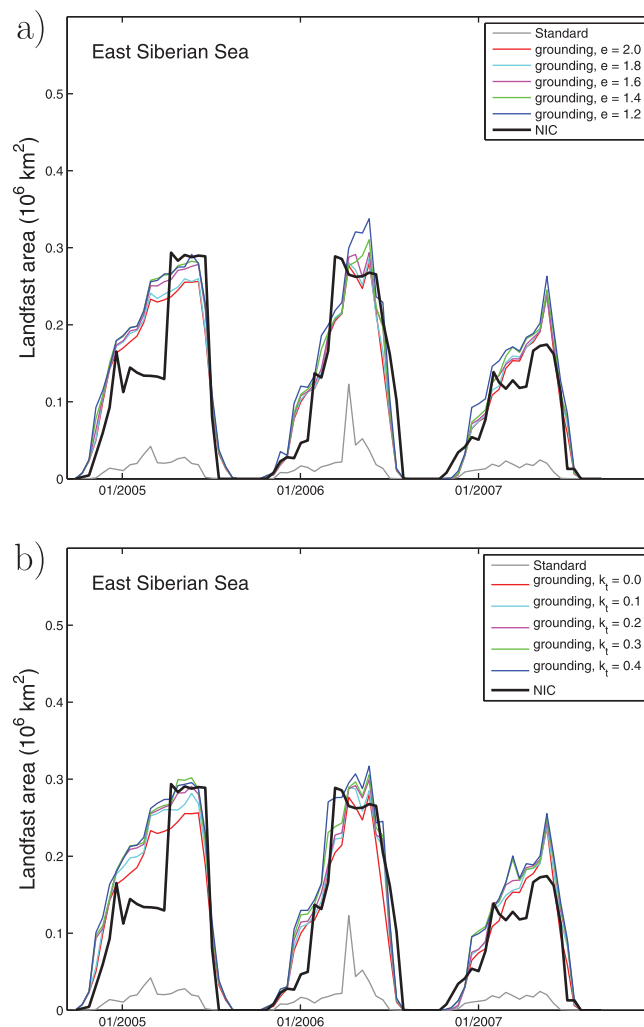
Figure 6. As in Figure 5a for the East Siberian Sea (a). As in Figure 5b for the East Siberian Sea (b).

Interestingly, for the East Siberian (Figure 6) and Laptev Seas (Figure 7), tensile strength has a more limited impact suggesting that grounding is the dominant mechanism. It is worth noting, however, that tensile strength improves the simulation of landfast ice in the Laptev Sea. Indeed, in the third year of the simulation, the landfast ice cover seems to be too weak in the simulation with grounding and with $e = 2$ and $k_t = 0$. On the other hand, $e = 1.6$ or $k_t = 0.1$ lead to reasonable fits to the data for this last year and even provide the best scores over the three landfast ice seasons when using our metric defined above (even though there is an overestimation of the landfast ice area in 2006).

6. Broader Implications

Our results indicate that increasing either uniaxial or isotropic tensile strength can improve the simulation of landfast ice in the Kara Sea and to a lesser extent in the Laptev Sea while having less impact in the East Siberian Sea. We found that for uniaxial tensile strength, the ellipse ratio should be between 1.4 and 1.6. For isotropic tensile strength, k_t should be between 0.1 and 0.2 to obtain the most realistic results. Figure 8 displays the frequency of occurrence for $e = 1.4$ (a and b) and $k_t = 0.2$ (c and d). These plots can be compared to the observed frequency of occurrence shown in Figure 4.

As k_t and e are the same everywhere on the domain in our experiments, the uniaxial and tensile strengths at a grid point only depend on the compressive strength which is a function of the ice thickness distribution [*Lipscomb et al.*, 2007]. However, intuitively, one would think that tensile strength should depend on other factors such as sea ice salinity, the ice temperature, the history of deformation of sea ice, etc. Near large Russian river mouths, it is possible that stronger ice is present as it is formed from fresher water. In order to simulate landfast ice, *Itkin et al.* [2015] used a k_t of 0.5 and doubled the ice strength parameter P^* only in regions shallower than 25 m. This was done by *Itkin et al.* [2015] to mimic the effect of grounding and to represent stronger coastal sea ice. As our model includes a grounding scheme and as we consider that the 25 m bathymetry limit is somehow arbitrary, k_t and e in our experiments are the same everywhere on the domain. As this modifies the rheology term, it not only has an impact on simulated landfast ice but also on the drift of pack ice.

To assess the impact of tensile strength on the drift of pack ice, we compared the simulated sea ice velocities against data from the International Arctic Buoy Program (IABP) [*Rigor and Ortmeyer*, 2004]. We want to focus on regions of drifting ice where the ice interactions (i.e., rheology) are important. To do so, we masked out regions where the observed frequency of occurrence of landfast ice (see Figure 4a) is larger than 0.01. We further extended this mask for all locations within 50 km of the initially masked points. Finally, marginal

Figure 7. As in Figure 5a for the Laptev Sea (a). As in Figure 5b for the Laptev Sea (b).

Seas (Baffin Bay, Greenland Sea, etc.) were also masked out in order to focus on the Arctic Ocean. Buoys in the regions defined by this mask were not considered for the analysis.

The IABP 12 hourly buoy positions have errors between 100 and 300 m depending on the buoy positioning system [*Thomas*, 1999]. We first obtained the monthly drift of IABP buoys by using the observed initial and final positions. We converted this distance into a monthly mean velocity ($\mathbf{u}_o$). For the simulations, the monthly mean velocity ($\mathbf{u}_s$) is calculated at the midpoint between the initial and final observed positions of a given buoy. It is obtained by doing a time average of the daily mean velocities $\mathbf{u_d}$. For a given month, N_o is the number of observed buoys used for this analysis. For each month, we computed the Root-Mean-Square Error (RMSE) =

$$\sqrt{\frac{1}{N_o}\sum_{n=1}^{N_o}|\mathbf{u}_s^n - \mathbf{u}_o^n|^2}$$ and the bias

$$= \frac{1}{N_o}\sum_{n=1}^{N_o}\left(|\mathbf{u}_s^n| - |\mathbf{u}_o^n|\right),$$ where the super-

script $n = 1, 2, \ldots N_o$ refers to the N_o observed buoys. The RMSE is a more comprehensive metric as it takes into account the errors/deviation in the drift direction. As a reference, the Polar Pathfinder Daily 25 km gridded sea ice velocity product [*Fowler et al.*, 2013] from the National Snow and Ice Data Center (NSIDC) is also evaluated against the IABP buoys.

Figure 9 shows these metrics as a function of time for the uniaxial tensile strength experiments. These results are consistent with what should be expected: as the shear strength increases, when the ellipse aspect ratio is reduced, the ice slows down. Note that a similar result is obtained with k_t: increasing the isotropic tensile strength leads to slower drifting ice (not shown). Interestingly, despite a more negative bias with $e = 1.4$, it leads to a slightly better RMSE (0.022 m s^{-1} over the 36 month period) than the one obtained with the standard $e = 2.0$ (0.024 m s^{-1}) suggesting that the drift direction is improved. A bootstrap method with replacement (10^5 iterations) confirms that this result is statistically significant with a confidence level of 99%. The simulated drift could be further improved by adjusting other parameters such as the ice-ocean drag parameter.

Ólason [2016] investigated the use of the standard elliptical yield curve (i.e., $e = 2$ and $k_t = 0$) and of a Coulombic yield curve [*Hibler and Schulson*, 2000] for simulating landfast ice in the Kara Sea. He has shown that with both yield curves it is possible to simulate landfast ice provided that they allow for some uniaxial tensile strength (which is the case with $e = 2$). As opposed to *Ólason* [2016], the area of landfast ice in our experiments is systematically too low with $e = 2$ (and $k_t = 0$). It is difficult to explain these different results. Is it due to the fact that the momentum equation in our simulations is solved with the EVP scheme as opposed to the implicit solver used by *Ólason* [2016]? *Ólason* [2016] claims that the numerical solution has to be sufficiently converged to simulate landfast ice with $e = 2$. *Ólason* [2016] also argues that Δ_{min} should
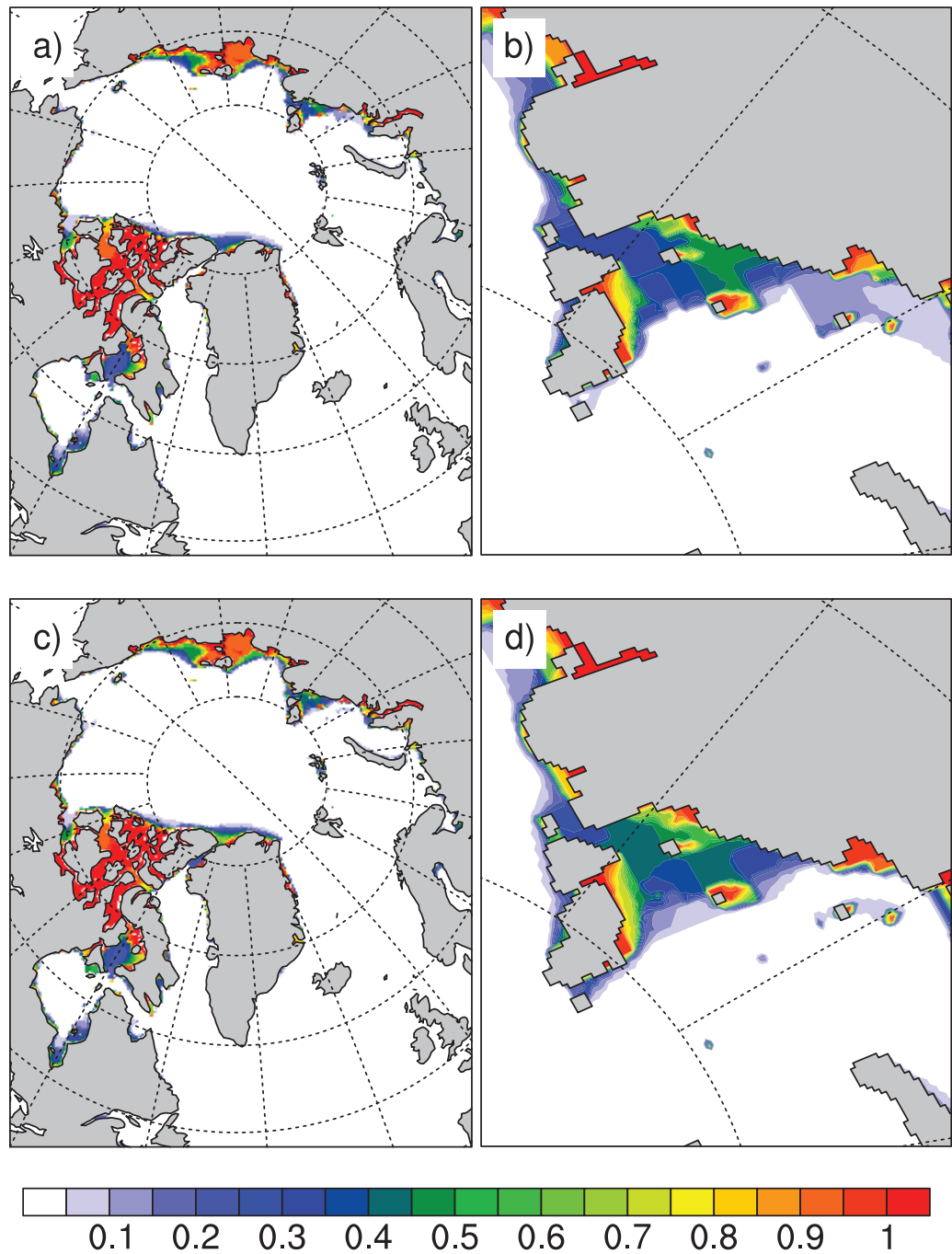
Figure 8. Frequency of occurrence of landfast ice for January–May for the years 2005, 2006, and 2007. $e = 1.4$ (a), $e = 1.4$ zoom in the eastern part of the Kara Sea (b), $k_t = 0.2$ (c), $k_t = 0.2$ (d), zoom in the eastern part of the Kara Sea. The grounding scheme was used for these simulations.

be set to a very low value (5×10^{-14} s^{-1}) but this was not explored in our study. Finally, is it possible that the two-thickness category model of *Ólason* [2016] leads to a stronger ice cover than the one simulated by the multithickness category CICE model?

Both our and his simulations (see his Figure 6) exhibit a shorter landfast ice season than observed. This is especially obvious at the onset of the landfast ice season: it happens later in the models than in the observations. As in the observations, our results and the simulations of *Ólason* [2016] exhibit rapid breakups of the landfast ice cover at the end of the season, but they tend to happen too early in the simulations. It is

Figure 9. Ice velocity against the IABP data. The gray curve is for the standard model ($e = 2$, $k_t = 0$, no grounding scheme). The red, cyan, magenta, green, and blue curves are for the grounding scheme, $k_t = 0$ and, respectively, for $e = 2.0$, 1.8, 1.6, 1.4, and 1.2. The bold black curve is for NSIDC.

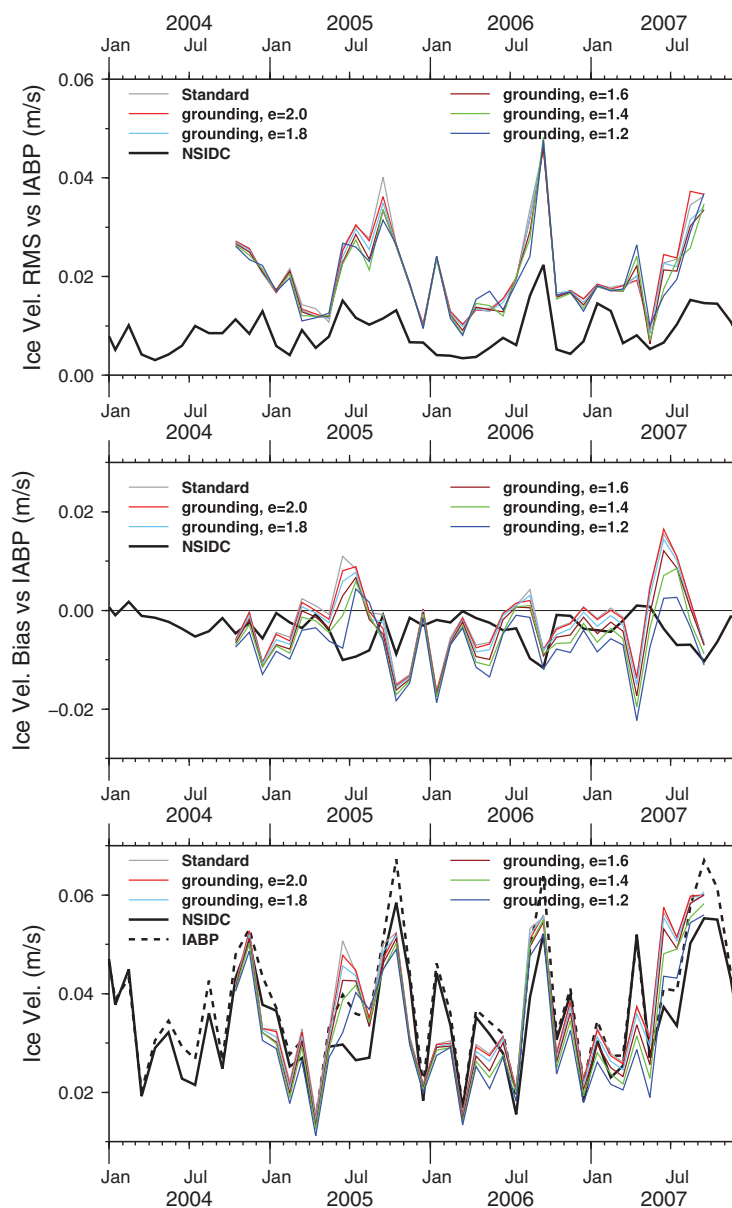unclear what can cause the too short simulated landfast ice season (mixed-layer depth for the initial growth, forcing, albedo parameterization, etc.).

Our results also demonstrate that landfast ice formation is a very nonlinear process. Figure 5a provides some evidence of this nonlinearity. Indeed, for the maximum landfast extent, the curves for $e = 2$, $e = 1.8$, and $e = 1.6$ follow each other while there is a big increase in the landfast ice area when decreasing e to 1.4. This is further illustrated by Figure 10 which shows the observed and simulated landfast ice covers on 23 April 2007. For $e = 1.6$ (or for larger values), the simulated landfast ice cover is very small and does not match the observations. However, decreasing e to 1.4 significantly improves the simulated landfast ice cover. $e = 1.2$ provides an even better simulated landfast ice cover for this specific date. We note that the model tends to exhibit landfast ice edges that are aligned with the grid (see, for example, Figure 10c). *Bouillon et al.* [2013] pointed out that the standard EVP solver sometimes leads to deformations that are aligned with the mesh.

Lemieux et al. [2015] mentioned that the landfast ice cover in the East Siberian Sea is characterized by modes: a small u-shaped mode following the shelf break and a larger mode extending into deeper water. Looking at the first landfast ice season in Figure 6 (2004–2005), one can see that the observations indicate that the small mode is present at the beginning of the season and that the large mode suddenly builds up and remains until the break up. The model (with $e = 1.6$, for example) correctly simulates this large mode but it occurs too early compared to observations.

At this stage, it is not clear if it is better to adjust the uniaxial or the isotropic tensile strength. In fact, it is possible that a combination of both would provide the best simulation of landfast ice but also of sea ice dynamics in general. More specific experiments and comparisons with observations should be performed in order to estimate the correct values for e and k_t. For example, if a landfast ice cover is observed along a flat coast with no islands nor anchor points offshore, isotropic tensile strength is required to maintain the ice in

Figure 10. Landfast ice (in blue) in the eastern part of the Kara Sea on 23 April 2007. NIC observations (a), simulation with $e = 1.6$ (b), simulation with $e = 1.4$ (c), and simulation with $e = 1.2$ (d). For all these simulations, $k_t = 0$ and the grounding scheme was used.

place in the presence of an offshore wind. The value of k_t could then be estimated. This is beyond the scope of this paper. It is worth noting, however, that some authors argue that isotropic tensile strength is around 1/20th of the compressive strength [e.g., *Hibler and Schulson*, 2000], which implies a k_t of 0.05 with the elliptical yield curve.

Miller et al. [2005] suggested that the simulated geophysical distribution of ice volume could be improved by increasing shear strength (they decreased the value of e). Our results and the ones of *Miller et al.* [2005] indicate that increasing tensile strength (and therefore shear strength) has the potential to improve the simulation of landfast ice, sea ice drift and sea ice thickness. This would, however, require further investigation.

This discussion should be further extended to what should be the most realistic yield curve for modeling sea ice and whether the VP rheological framework is appropriate for modeling landfast ice and sea ice dynamics in general. Although most sea ice models nowadays are based on a VP formulation with an

elliptical yield curve, other yield curves, inspired by other fields [e.g., *Ip et al.*, 1991], derived from laboratory experiments [*Hibler and Schulson*, 2000] and remote sensing observations [*Wang*, 2007], have been proposed. Other rheology frameworks based on elastic formulations have also been presented [*Schreyer et al.*, 2006; *Girard et al.*, 2011]. How rheology should be represented in a sea ice model remains the subject of intense research and debate.

7. Concluding Remarks

Lemieux et al. [2015] recently introduced a parameterization to represent the effect of grounded ridges on sea ice dynamics. Used with a VP sea ice model, the parameterization clearly improves the simulation of landfast ice in regions such as the East Siberian Sea, the Laptev Sea and along the coast of Alaska. However, in some regions such as the Kara Sea, the area of landfast ice is systematically underestimated. This is explained by the fact that, compared to the Laptev Sea, for example, the Kara Sea is overall too deep for ridges to reach the seafloor. *Ólason* [2016] argues that ice arching is the main mechanism responsible for the Kara Sea landfast ice cover. In order to promote ice arching, we have modified the uniaxial or the isotropic tensile strength of the VP elliptical yield curve. Both uniaxial and isotropic tensile strengths improve the simulation of landfast ice in the Kara Sea (with also a smaller improvement in the Laptev Sea). Nevertheless, our numerical experiments lead to a landfast ice season for the Kara Sea that is too short when compared to observations. This is especially obvious at the onset of the landfast ice season: it systematically occurs later in the model and the simulated area of landfast ice exhibits a slower build up than the observed one. This indicates that processes related to sea ice thermodynamics should also be considered in order to improve our simulation of landfast ice.

In this paper, we mostly discussed the simulation of landfast ice along the Siberian coast. Our results demonstrated that the simulation of landfast ice can be improved by using a grounding scheme and adjusting the tensile strength. However, there are regions where the model simulates too much landfast ice with any of the parameters tested (see, for example, Figure 4c). This is the case for example in Prince Regent Inlet, the Gulf of Boothia and Foxe Basin. As these regions are characterized by strong tidal signals, we speculate that including tides would decrease the simulated area of landfast ice for these zones. To investigate this, we are currently developing a high-resolution (1/12°) ice-ocean model with tides. As future work, we also plan to develop a more sophisticated grounding scheme based on the ice thickness distribution.

References

Bouillon, S., T. Fichefet, V. Legat, and G. Madec (2013), The elastic-viscous-plastic method revisited, *Ocean Model.*, *71*, 2–12, doi:10.1016/j.ocemod.2013.05.013.

Divine, D. V., R. Korsnes, A. P. Makshtas, F. Godtliebsen, and H. Svendsen (2005), Atmospheric-driven state transfer of shore-fast ice in the northeastern Kara Sea, *J. Geophys. Res.*, *110*, C09013, doi:10.1029/2004JC002706.

Dumont, D., Y. Gratton, and T. E. Arbetter (2009), Modeling the dynamics of the North Water polynya ice bridge, *J. Phys. Oceanogr.*, *39*, 1448–1461, doi:10.1175/2008JPO3965.1.

Dupont, F., S. Higginson, R. Bourdallé-Badie, Y. Lu, F. Roy, G. C. Smith, J.-F. Lemieux, G. Garric, and F. Davidson (2015), A high-resolution ocean and sea-ice modelling system for the Arctic and the North Atlantic oceans, *Geosci. Model Dev.*, *8*, 1577–1594, doi:10.5194/gmd-8-1577-2015.

Ferry, N., et al. (2012), Glorys2v1 global ocean reanalysis of the altimetric era (1993-2009) at meso scale, *Mercator Ocean Quat. Newsl.*, *44*, 28–39.

Fowler, C., W. Emery, and M. Tschudi (2013), Polar Pathfinder Daily 25 km EASE-Grid Sea Ice Motion Vectors, version 2, Natl. Snow and Ice Data Cent., Boulder, Colo.

Girard, L., S. Bouillon, J. Weiss, D. Amitrano, T. Fichefet, and V. Legat (2011), A new modeling framework for sea-ice mechanics based on elasto-brittle rheology, *Ann. Glaciol.*, *52*(57), 123–132.

Goldstein, R. V., N. N. Osipenko, M. Leppäranta, P. Mäntyniemi, J. Seppänen, M. Nieminen, and E. Kärkäs (2004), On the shape of the fast ice-drift ice contact zone, *Geophysica*, *40*(1-2), 3–13.

Haas, C., W. Dierking, T. Busche, and J. Hoelemann (2005), Envisat ASAR monitoring of polynya processes and sea ice production in the Laptev Sea, in Proceedings of the 2004 Envisat & ERS Symposium (ESA SP-572), edited by H. Lacoste and L. Ouwehand, ESA Publications Division, Netherlands.

Hibler, W. D. (1979), A dynamic thermodynamic sea ice model, *J. Phys. Oceanogr.*, *9*, 815–846.

Hibler, W. D., and E. M. Schulson (2000), On modeling the anisotropic failure and flow of flawed sea ice, *J. Geophys. Res.*, *105*(C7), 17,105–17,120.

Hunke, E. C. (2001), Viscous-plastic sea ice dynamics with the EVP model: Linearization issues, *J. Comput. Phys.*, *170*, 18–38.

Hunke, E. C., and W. H. Lipscomb (2008), CICE: The Los Alamos sea ice model. Documentation and software user's manual version 4.0, *Tech. Rep. LA-CC-06-012*, Los Alamos Natl. Lab., Los Alamos, N. M.

Ip, C. F. (1993), Numerical investigation of different rheologies on sea-ice dynamics, PhD thesis, Darmouth Coll., Hanover, N. H.

Ip, C. F., W. D. Hibler, and G. M. Flato (1991), On the effect of rheology on seasonal sea-ice simulations, *Ann. Glaciol.*, *15*, 17–25.

Itkin, P., M. Losch, and R. Gerdes (2015), Landfast ice affects the stability of the Arctic halocline: Evidence from a numerical model, *J. Geophys. Res.*, *120*, 2622–2635, doi:10.1002/2014JC010353.

Johnson, M., et al. (2012), Evaluation of Arctic sea ice thickness simulated by Arctic Ocean Model Intercomparion Project models, *J. Geophys. Res.*, *117*, C00D13, doi:10.1029/2011JC007257.

König Beatty, C., and D. M. Holland (2010), Modeling landfast sea ice by adding tensile strength, *J. Phys. Oceanogr.*, *40*, 185–198, doi:10.1175/2009JPO4105.1.

Lemieux, J.-F., L. B. Tremblay, F. Dupont, M. Plante, G. C. Smith, and D. Dumont (2015), A basal stress parameterization for modeling landfast ice, *J. Geophys. Res. Oceans*, *120*, 3157–3173, doi:10.1002/2014JC010678.

Lipscomb, W. H., E. C. Hunke, W. Maslowski, and J. Jakacki (2007), Ridging, strength, and stability in high-resolution sea ice models, *J. Geophys. Res.*, *112*, C03S91, doi:10.1029/2005JC003355.

Mahoney, A., H. Eicken, and L. Shapiro (2007), How fast is landfast sea ice? A study of the attachment and detachment of nearshore ice at Barrow, Alaska, *Cold Reg. Sci. Technol.*, *47*, 233–255, doi:10.1016/j.coldregions.2006.09.005.

Mahoney, A. R., H. Eicken, A. G. Gaylord, and R. Gens (2014), Landfast sea ice extent in the Chukchi and Beaufort Seas: The annual cycle and decadal variability, *Cold Reg. Sci. Technol.*, *103*, 41–56, doi:10.1016/j.coldregions.2014.03.003.

Megann, A., D. Storkey, Y. Aksenov, S. Alderson, D. Calvert, T. Graham, P. Hyder, J. Siddorn, and B. Sinha (2014), GO5.0: The joint NERC-Met Office NEMO global ocean model for use in coupled and forced applications, *Geosci. Model Dev.*, *7*, 1069–1092, doi:10.5194/gmd-7-1069-2014.

Miller, P. A., S. W. Laxon, and D. L. Feltham (2005), Improving the spatial distribution of modeled Arctic sea ice thickness, *Geophys. Res. Lett.*, *32*, L18503, doi:10.1029/2005GL023622.

National Ice Center (2006), *National Ice Center Arctic Sea Ice Charts and Climatologies in Gridded Format*, edited and compiled by F. Fetterer and C. Fowley, Natl. Snow and Ice Data Cent., Boulder, Colo., doi:10.7265/N5X34VDB. [Available at http://nsidc.org/data/g02172/.]

Ólason, E. (2016), A dynamical model of Kara Sea land-fast ice, *J. Geophys. Res. Oceans*, *121*, 3141–3158, doi:10.1002/2016JC011638.

Rigor, I. G., and M. Ortmeyer (2004), The International Arctic Buoy Programme—Monitoring the Arctic ocean for forecasting and research, *Arctic Res. U.S.*, *18*, 21–25.

Roy, F., M. Chevallier, G. C. Smith, F. Dupont, G. Garric, J.-F. Lemieux, Y. Lu, and F. Davidson (2015), Arctic sea ice and freshwater sensitivity to the treatment of the atmosphere-ice-ocean surface layer, *J. Geophys. Res. Oceans*, *120*, 4392–4417, doi:10.1002/2014JC010677.

Schreyer, H. L., D. L. Sulsky, L. B. Munday, M. D. Coon, and R. Kwok (2006), Elastic-decohesive constitutive model for sea ice, *J. Geophys. Res.*, *111*, C11S26, doi:10.1029/2005JC003334.

Smith, G. C., F. Roy, P. Mann, F. Dupont, B. Brasnett, J.-F. Lemieux, S. Laroche, and S. Bélair (2014), A new atmospheric dataset for forcing ice-ocean models: Evaluation of reforecasts using the Canadian global deterministic prediction system, *Q. J. R. Meteorol. Soc.*, *140*(680), 881–894, doi:10.1002/qj.2194.

Thomas, D. (1999), The quality of sea ice velocity estimates, *J. Geophys. Res.*, *104*(C6), 13,627–13,652.

Vancoppenolle, M., S. Bouillon, T. Fichefet, H. Goosse, O. Lecomte, M. A. Morales Maqueda, and G. Madec (2012), LIM, The Louvain-la-Neuve sea ice model, Notes du Pôle de modélisation, 31.

Wang, K. (2007), Observing the yield curve of compacted pack ice, *J. Geophys. Res.*, *112*, C05015, doi:10.1029/2006JC003610.

Yu, Y., H. Stern, C. Fowler, F. Fetterer, and J. Maslanik (2014), Interannual variability of Arctic landfast ice between 1976 and 2007, *J. Clim.*, *27*, 227–243, doi:10.1175/JCLI-D-13-00178.1.